Understanding transport phenomena in electrochemical energy devices via X-ray nano CT

2017 J. Phys.: Conf. Ser. 849 012018

(http://iopscience.iop.org/1742-6596/849/1/012018)

IOP Conf. Series: Journal of Physics: Conf. Series **849** (2017) 012018 doi:10.1088/1742-6596/849/1/012018

Understanding transport phenomena in electrochemical energy devices via X-ray nano CT

B Tjaden[1], J Lane[2], D J L Brett[1], P R Shearing[1,*]

[1]Electrochemical Innovation Lab, Department of Chemical Engineering, University College London, WC1E 7JE, UK
[2]Praxair Inc., 175 E. Park Dr., Tonawanda, NY 14150, USA
*Corresponding author: e-mail: p.shearing@ucl.ac.uk

Abstract. Porous support layers in electrochemical devices ensure mechanical stability of membrane assemblies such as solid oxide fuel cells and oxygen transport membranes (OTMs). At the same time, porous layers affect diffusive mass transport of gaseous reactants and contribute to performance losses at high fuel utilisation and conversion ratios. Microstructural characteristics are vital to calculate mass transport phenomena, where tortuosity remains notoriously difficult to determine. Here, the tortuosity of tubular porous support layers of OTMs is evaluated via high resolution X-ray nano computed tomography. The high resolution reveals the complex microstructure of the samples to then execute a selection of image-based tortuosity calculation algorithms. Visible differences between geometric and flux-based algorithms are observed and have thus to be applied with caution.

1. Introduction

Electrochemical energy devices have the potential to revolutionize distributed low-carbon power supply. However, in order to optimise their performance and enhance durability, a much improved understanding of the underlying material microstructure is required. In particular, the rate limiting step of fuel cells and oxygen transport membranes (OTMs) is governed by mass transport resistance in porous media, which, in turn, is a function of microstructural characteristics such as tortuosity, porosity and mean pore diameter [1]. These parameters are interrelated in a complicated manner [2].

Here, we utilise high resolution X-ray nano computed tomography (X-ray nano CT) to reveal the complex microstructure and resolve geometric features affecting the mass transport within tubular porous support layers of OTMs. Among the aforementioned parameters, tortuosity remains notoriously difficult to calculate [3]. Geometrically, tortuosity (τ) is calculated by dividing the shortest path length through a structure (Δl) by the Euclidean distance between the two endpoints of that path (Δx). However, in transport problems, the tortuosity in combination with the porosity (ε), is also applied to relate the effective transport property (D_{eff}) within a structure to its bulk transport property (D_{bulk}). Eq. (1) and Eq. (2) present both expressions, respectively.

$$\tau = \frac{\Delta l}{\Delta x} \qquad \text{Eq. (1)}$$

$$D_{eff} = \frac{\varepsilon}{\tau^2} D_{bulk} \qquad \text{Eq. (2)}$$

This work compares a wide range of frequently used image-based tortuosity calculation approaches. These approaches are subdivided into geometric-based and flux-based algorithms, according to the differentiation shown in the above equations. Their suitability for quantifying diffusive mass transport in porous structures is then assessed.

2. Methodology

Four tubular yttria partially-stabilized zirconia porous support membrane samples for the application in OTMs were prepared for X-ray tomography. The samples differed in sintering temperature and wall thickness as listed in Table 1.

Table 1: Description of analysed samples.

Sample ID	Wall thickness	Sintering temperature
PS 1400 1.3	1.3 mm	1,400 °C
PS 1400 1.0	1.0 mm	1,400 °C
PS 1450 1.3	1.3 mm	1,450 °C
PS 1450 1.0	1.0 mm	1,450 °C

Table 2: Imaging specifications for X-ray nano CT.

Field of view	65 µm
Camera binning	1
Pixel size	63.1 nm
Exposure time	90 s
X-ray energy	5.4 keV
Number of images	901

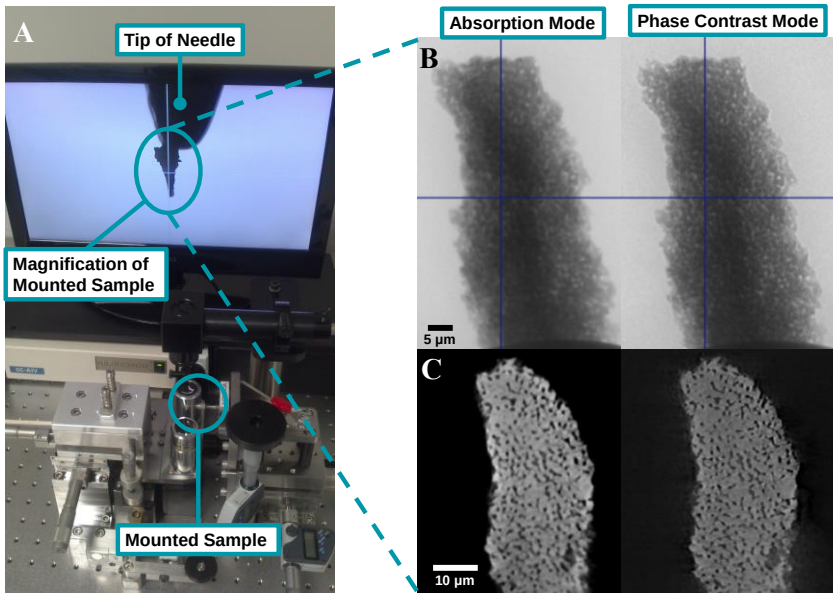

Figure 1: Mounted sample ready for X ray CT (A); radiographs (B) and image slices (C) comparing the phase and absorption imaging mode.

X-ray nano CT using the Zeiss Xradia 810 Ultra was applied to reconstruct the samples in 3D, where the imaging specifications for each sample were identical, as presented in Table 2. The Zeiss Xradia 810 Ultra achieves a quasi-monochromatic X-ray beam of 5.4 keV by the use of X-ray optics: the combination of a capillary condenser and a Fresnel zone plate filter out X-rays with energies above and below the K-edge of the chromium target and focus the beam onto the sample and detector. Figure 1A shows the small sample size of < 65 µm necessary to avoid artefacts during imaging. The Zeiss Xradia Ultra 810 is capable of imaging in absorption as well as in Zernike phase contrast mode [4]. Both modes were evaluated for their achieved image quality as shown in Figure 1B and C. It is visible that the edges and boundaries of the solid phase are finer and better defined in phase contrast mode. Hence, phase contrast imaging was chosen over absorption imaging despite the highly attenuating sample materials.

After reconstruction using a standard filtered back projection algorithm (XRM Reconstructor), the image datasets were segmented using threshold segmentation and two volumes of different dimensions were cropped for each sample to verify the consistency of results: a cube with a side length of 6.31 µm and a cuboid with the side lengths of 6.31 µm × 6.31 µm × 12.62 µm. The tortuosity was then calculated

via a range of computational algorithms executed across these volumes: the fast marching method (FMM) [5], the built-in Avizo (FEI) module "Centriod Path Tortuosity" [6], by simulating the heat flux in StarCCM+ (CD-adapco) [7–9] and mass flux in COMSOL Multiphysics (COMSOL Inc.) as well as via a MATLAB based Laplace equation solver called "TauFactor" [10, 11]. While the first two calculation algorithms calculate tortuosity geometrically by applying Eq. (1), the latter three approaches simulate a flux and correlate the effective transport properties to the bulk transport properties via Eq. (2). These algorithms arrive at distinct tortuosity values along each axis of the volume and, hence, the characteristic tortuosity (τ_C) [7] was calculated for each sample. Moreover, well-known porosity-tortuosity relationships, including the Bruggeman relationship [12] and the Maxwell relationship [13], were used for comparative reasons.

3. Results and Discussion

Table 3 compares microstructural characteristics for each of the eight extracted sample volumes. The porosity was calculated via the pixel counting method while the pore diameter was achieved using the continuous pore size distribution code from [14]. It is evident that samples with lower sintering temperature feature larger pore diameter and porosity, favouring diffusive mass transport.

Table 3: Microstructural characteristics of each sample volume.

Sample ID		d_P [µm]	ε [-]
PS 1400 1.3	Cube	0.73	0.31
	Cuboid	0.74	0.32
PS 1400 1.0	Cube	0.71	0.34
	Cuboid	0.70	0.32
PS 1450 1.0	Cube	0.66	0.25
	Cuboid	0.65	0.24
PS 1450 1.3	Cube	0.63	0.23
	Cuboid	0.63	0.21

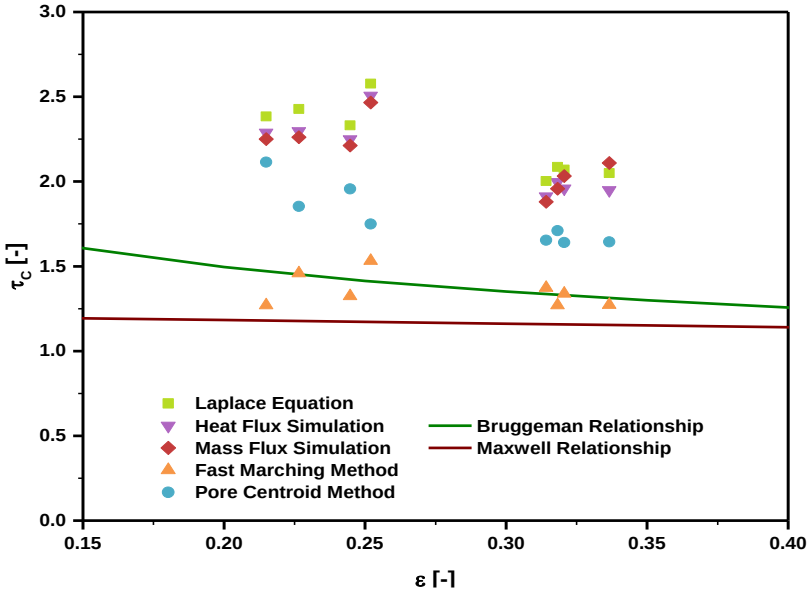

Figure 2: Comparison of tortuosity calculation algorithms which show the difference in geometric and flux-based algorithms. Empirical relationships such as the Bruggeman and Maxwell relation are unfit for the analysed microstructure treated here.

Figure 2 shows the characteristic tortuosity values of both geometric-based algorithms and of all three flux-based algorithms, similar as in [7]. The FMM achieved the lowest tortuosity values among all algorithms with the pore centroid method results slightly above. However, the former approach has the least significance in analysing the tortuosity of the porous phase. The algorithm locates the pore centroid of each slice and follows it in the in-plane direction. Hence, this algorithm is considered only

as an indicator for the homogeneity of the porous phase within the sample: the centroid of a homogeneous sample will be located closer to the centre of each image slice and thus, the resulting tortuosity will be closer to unity. The low porosity samples feature a higher pore centroid tortuosity, suggesting a higher heterogeneity in the microstructure. Both empirical relationships form the lower boundary of tortuosity, where the FMM achieved values around the Bruggeman correlation. All tortuosity algorithms broadly followed the trend of decreasing tortuosity with increasing porosity.

The results of the three flux-based algorithms were very close to each other, with values around 2.3 for the low porosity samples and around 1.9 for the high porosity samples. The Laplace equation solver achieved slightly higher values compared to the other simulation-based algorithms, which might be caused by some minor smoothing effects during mesh generation for the flux simulations.

The visible differences between the FMM and the flux-based algorithms were caused by the lack of the FMM to account for constrictions and bottlenecks while only considering the minimal Euclidean distance between two planes. Hence, any pore connection, even a single pixel, was included in the calculation and thus, the geometric definition of tortuosity is closely followed. However, a migrating flux is affected by the variation of pore diameters within the sample and choses the path of least resistance and constriction. As a consequence, flux-based tortuosity calculation algorithms always result in a higher tortuosity value. In the presented study, this difference amounts to almost a factor of two. Thus, when calculating the effective transport property of a transport phenomenon following Eq. (2), a flux-based tortuosity computation algorithm has to be applied to correctly cater for the effect of the microstructure on the transport process. Among the included flux-based tortuosity calculation methods, the Laplace equation solver produced consistent results and is easiest to execute, as the binarized image sequence is sufficient as input file, making the generation of a volume mesh unnecessary.

4. Conclusions

X-ray nano CT was used to reveal the complex microstructure of porous support membranes and evaluate the effect of microstructural characteristics on transport phenomena. The high resolution allowed the execution of a wide range of tortuosity calculation approaches, where the high number of different algorithms is testimony of the importance of tomography techniques in analysing transport processes in porous structures. Significant differences between geometric and flux-based algorithms were observed. The reason for this is that geometric approaches do not take constrictions and bottlenecks into account, which affect the migration path of a flux. Consequently, care must be taken when comparing tortuosity values calculated via algorithms following different concepts.

References

[1] Shearing P R, Brett D J L and Brandon N P 2013 *Int. Mater. Rev.* **55** 347–63
[2] Shearing P R, Howard L E, Jørgensen P S, Brandon N P and Harris S J 2010 *Electrochem. Commun.* **12** 374–7
[3] Tjaden B, Brett D J L and Shearing P R 2016 *Int. Mater. Rev.*
[4] Holzner C, Feser M, Vogt S, Hornberger B, Baines S B and Jacobsen C 2010 *Nat Phys* **6** 883–7
[5] Jørgensen P S, Hansen K V, Larsen R and Bowen J R 2011 *J. Microsc.* **244** 45–58
[6] Gostovic D, Smith J R, Kundinger D, Jones K S and Wachsman E D 2007 *Electrochem. Solid-State Lett.* **10** B214-7
[7] Cooper S J, Kishimoto M, Tariq F, Bradley R S, Marquis A J, Brandon N P, Kilner J A and Shearing P R 2013 *ECS Trans.* **57** 2671–8
[8] Trogadas P, Taiwo O O, Tjaden B, Neville T P, Yun S, Parrondo J, Ramani V, Coppens M-C, Brett D J L and Shearing P R 2014 *Electrochem. Commun.* **48** 155–9
[9] Tjaden B, Lane J, Withers P J, Bradley R S, Brett D J L and Shearing P R 2016 *Solid State Ionics* **288** 315–21
[10] Cooper S J, Bertei A, Shearing P R, Kilner J A and Brandon N P 2016 *SoftwareX*.

[11] Finegan D P, Cooper S J, Tjaden B, Taiwo O O, Gelb J, Hinds G, Brett D J L and Shearing P R 2016 *J. Power Sources* **333** 184–92.
[12] Tjaden B, Cooper S J, Brett D J L, Kramer D and Shearing P R 2016 *Curr. Opin. Chem. Eng.* **12** 44–51
[13] Chueh C C, Bertei A, Pharoah J G and Nicolella C *Int. J. Heat Mass Transfer 2014* **71** 183–8
[14] Münch B and Holzer L *J. Am. Ceram. Soc.* 2008 **91** 4059–67